



HAL
open science

Relationship between magnetic ordering and gigantic magnetocaloric effect in HoB₂ studied by neutron diffraction experiment

Noriki Terada, Kensei Terashima, Pedro Baptista de Castro, Claire Colin, Hiroaki Mamiya, Takafumi D Yamamoto, Hiroyuki Takeya, Osamu Sakai, Yoshihiko Takano, Hideaki Kitazawa

► To cite this version:

Noriki Terada, Kensei Terashima, Pedro Baptista de Castro, Claire Colin, Hiroaki Mamiya, et al.. Relationship between magnetic ordering and gigantic magnetocaloric effect in HoB₂ studied by neutron diffraction experiment. *Physical Review B*, 2020, 102 (9), pp.094435. 10.1103/physrevb.102.094435 . hal-04143410

HAL Id: hal-04143410

<https://hal.science/hal-04143410>

Submitted on 27 Jun 2023

HAL is a multi-disciplinary open access archive for the deposit and dissemination of scientific research documents, whether they are published or not. The documents may come from teaching and research institutions in France or abroad, or from public or private research centers.

L'archive ouverte pluridisciplinaire **HAL**, est destinée au dépôt et à la diffusion de documents scientifiques de niveau recherche, publiés ou non, émanant des établissements d'enseignement et de recherche français ou étrangers, des laboratoires publics ou privés.

Relationship between magnetic ordering and gigantic magnetocaloric effect in HoB₂ studied by neutron diffraction experiment

Noriki Terada¹,¹ Kensei Terashima,¹ Pedro Baptista de Castro,^{1,2} Claire V. Colin,³ Hiroaki Mamiya,¹ Takafumi D. Yamamoto,¹ Hiroyuki Takeya,¹ Osamu Sakai,⁴ Yoshihiko Takano,^{1,2} and Hideaki Kitazawa¹

¹National Institute for Materials Science, Sengen 1-2-1, Tsukuba, Ibaraki 305-0047, Japan

²University of Tsukuba, 1-1-1 Tennodai, Tsukuba, Ibaraki, 305-8577, Japan

³Université Grenoble Alpes, CNRS, Institut Néel, 38042 Grenoble, France

⁴Neutron Science and Technology Center, Comprehensive Research Organization for Science and Society, Tokai Ibaraki 319-1106, Japan



(Received 30 June 2020; revised 20 August 2020; accepted 15 September 2020; published 28 September 2020)

Recently, HoB₂ was discovered to undergo a gigantic magnetic entropy change; the largest $|\Delta S_M| = 40.1 \text{ J kg}^{-1} \text{ K}^{-1}$ ($0.35 \text{ J cm}^{-3} \text{ K}^{-1}$) in magnetocaloric materials studied for hydrogen liquefaction [P. Baptista de Castro *et al.*, NPG Asia Mater. **12**, 35 (2020)]. In this study, in order to investigate the origin of the gigantic $|\Delta S_M|$ in HoB₂, we studied the magnetic orderings by neutron diffraction with an enriched powder sample of Ho¹¹B₂. Our experimental results showed the onset of ferromagnetic long-range order below $T_C = 15 \text{ K}$. For the second phase transition at $T_2 = 11 \text{ K}$, the spin reorientation occurs, and the temperature dependence of the total magnetic moment of Ho³⁺ shows a kink anomaly, which is typically seen in compounds with quadrupolar ordering. In addition, the temperature dependence of the ferromagnetic short-range order above T_C is strongly related to that of the magnetic entropy change in HoB₂. These results infer that the gigantic $|\Delta S_M|$ in HoB₂ is caused by (i) the spin reorientation transition, which is likely associated with quadrupolar ordering, giving the additional contribution to $|\Delta S_M|$ at the lower phase transition temperature, $T_2 = 11 \text{ K}$, and (ii) the large FM fluctuation above T_C with origins in the strong suppression of the FM long-range order.

DOI: [10.1103/PhysRevB.102.094435](https://doi.org/10.1103/PhysRevB.102.094435)

I. INTRODUCTION

In the past 20 years, the magnetocaloric effect (MCE) in the low-temperature range has attracted increasing attention, driven by the demand for hydrogen liquefaction at a condensation temperature of 20.3 K [1,2]. In this regard, rare-earth intermetallic compounds are expected to be good candidate magnetocaloric materials because of their large magnetic moment and high density; for example, ErCo₂ and HoAl₂ both undergo large magnetic entropy changes, $|\Delta S_M| = 36$ and $28.8 \text{ J kg}^{-1} \text{ K}^{-1}$, when a magnetic field of 5 T is applied [3,4].

Recently, HoB₂ was discovered to undergo a gigantic magnetic entropy change; the largest $|\Delta S_M| = 40.1 \text{ J kg}^{-1} \text{ K}^{-1}$ ($0.35 \text{ J cm}^{-3} \text{ K}^{-1}$) at 15 K by a magnetic field change of 5 T in all the MCE materials that have been studied for hydrogen liquefaction [5]. HoB₂ is a rare-earth diboride RB₂, where R is a rare-earth ion; it has an AlB₂-type crystal structure in the space group *P6/mmm*, as illustrated in Fig. 1. The diborides RB₂ ($R = \text{Tb, Er, Tm}$) exhibit a simple ferromagnetic (FM) phase transition from the paramagnetic phase, with the Curie temperature T_C depending on the rare-earth ion [6–8]. By contrast, DyB₂ and HoB₂ have been reported to show two phase transitions, where the higher phase transition is associated with a FM-paramagnetic phase transition. The lower phase transition in DyB₂ was suggested to be a spin-reorientation-like transition [9]. However, the origin of the lower transition in both cases has not been clarified thus far.

The $|\Delta S_M|$ values of RB₂ ($R = \text{Tb, Dy}$) were reported previously; that is, the $|\Delta S_M|$ values of TbB₂ and DyB₂ are

~ 10 and $17 \text{ J kg}^{-1} \text{ K}^{-1}$ for $\mu_0 \Delta H = 5 \text{ T}$, respectively [6,9]. Compared with these rare-earth diborides, the MCE of HoB₂ is unexpectedly large. In this study, we investigate the relationship between the magnetic orderings and the gigantic MCE in HoB₂ by using a neutron diffraction experiment.

II. EXPERIMENTAL DETAILS

A polycrystalline sample of HoB₂ was synthesized by an arc-melting process in a water-cooled copper hearth arc furnace. Stoichiometric amounts of Ho (99.9% purity) and the ¹¹B enriched isotope (99.5%) were melted in an argon atmosphere. The as-cast sample vacuum sealed in a quartz tube was heat treated at 1000 °C for 7 days for homogenization and then quenched in water. In order to determine the sample quality, we used the powder x-ray diffraction technique. We confirmed that the main phase was HoB₂ for the heat-treated sample. Small amounts of the impurity phases HoB₄ and Ho₂O₃ were also detected, with the volume fractions being approximately 5% and 2%, respectively. These impurities show antiferromagnetic phase transition at $T = 7.1 \text{ K}$ in HoB₄ [10] and at $T = 2 \text{ K}$ in Ho₂O₃ [11], which are different from the phase transition temperatures of HoB₂. Samples were powdered using an agate mortar and stored in vanadium cylinders for the neutron powder diffraction experiments.

The neutron diffraction experiment was carried out with a two-axis diffractometer on D1B at the Institut Laue Langevin in Grenoble, France [12]. An incident neutron wavelength of

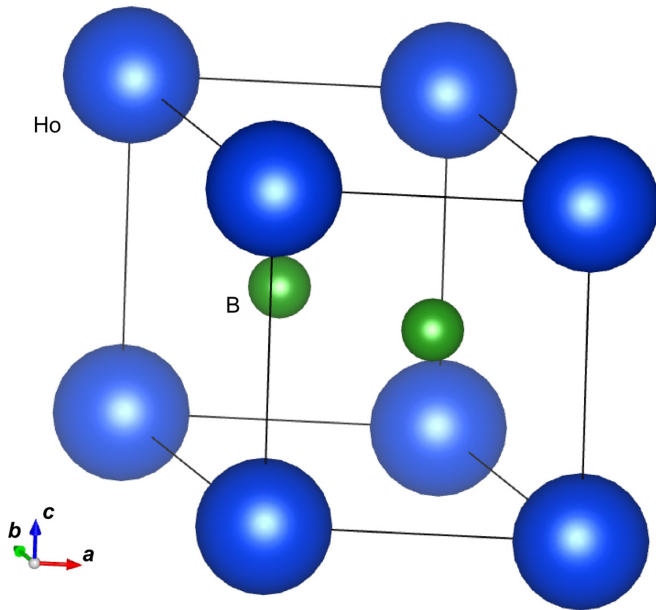


FIG. 1. Illustration of crystal structure of HoB_2 . Ho is placed at Wyckoff position 1a (0,0,0), and B is at 2d ($1/3, 2/3, 1/2$) in space group $P6/mmm$. The lattice constants are $a = b = 3.2849(8)$ Å, $c = 3.8183(16)$ Å at room temperature.

2.52 Å was employed. We used a standard liquid He cryostat to cool the sample. The powder sample was put into a cylindrical V sample holder. The magnetic structure analysis, including Rietveld refinement, was carried out using the FULLPROF SUITE program [13]. We also used the magnetic properties measurement system manufactured by the company Quantum Design (QD) to compare the neutron data with the magnetic entropy change estimated from the magnetization data. The specific heat measurement was carried out with QD's physical properties measurement system.

III. EXPERIMENTAL RESULTS

A. Ferromagnetic long-range order

As shown in Fig. 2, certain reflections appear below $T_C = 15$ K. All additional reflections are placed on the $P6/mmm$ symmetry-allowed positions. Considering that the unit cell contains one magnetic Ho atom, the onset of FM ordering could be concluded to occur below 15 K in HoB_2 . The magnetic propagation vector is determined to be $\mathbf{k} = (0, 0, 0)$, which means that the magnetic unit cell is identical to the crystal lattice. We confirmed that the additional reflections are not caused by a crystal lattice distortion by testing possible lattice distortions, including the orthorhombic subgroup $Cmmm$. As shown in Fig. 3(a), the integrated intensity of the magnetic 100 reflection appears below $T = 15$ K. The temperature dependence of this intensity shows a kink anomaly at the second phase transition at $T = 11$ K ($\equiv T_2$), as indicated by the arrow in Fig. 3(a). The specific heat also shows a peak anomaly at $T = 11$ K, which is shown in Fig. 3(d). Moreover, the temperature dependences of the intensity of the 100 and 001 reflections do not conform to each other [Fig. 3(a)]; for example, the intensity ratio I_{001}/I_{100} is 0.78(3) at $T = 12.0$ K

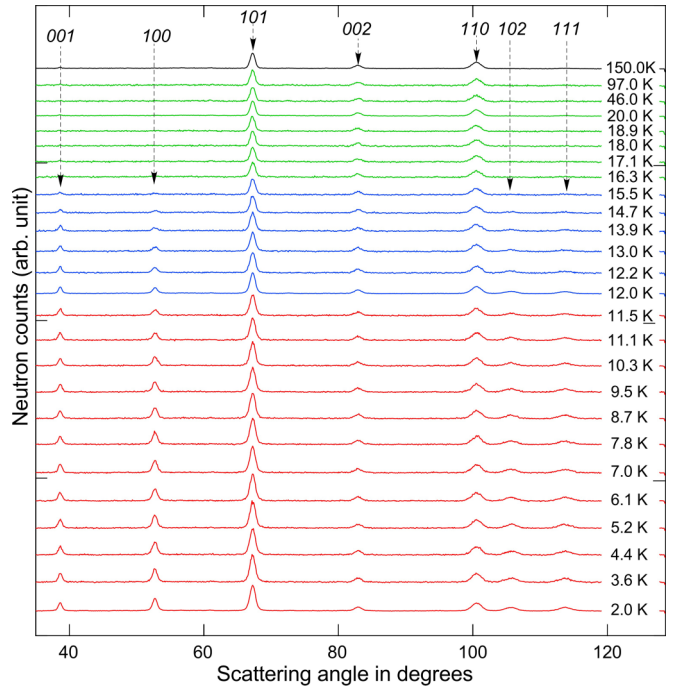


FIG. 2. Temperature dependence of the powder neutron diffraction pattern in HoB_2 .

and 0.51(2) at $T = 2.0$ K. This indicates that the direction of the magnetic moment of the FM structure depends on temperature, which will be described shortly.

To determine the precise spin direction, we performed Rietveld refinements for the data below $T = 15$ K. The $P6/mmm$ space group contains two magnetic irreducible representations (IRs), namely, $m\Gamma_2^+$ and $m\Gamma_6^+$ [14]. The $m\Gamma_2^+$ representation confines spins along the c axis, whereas $m\Gamma_6^+$ has three different distortion modes, in which the spins occur along $[100]$ or $[1\bar{1}0]$ or in any direction in the ab plane. The neutron diffraction experiment with the powder sample did not allow the spin direction in the basal plane to be determined in the case of hexagonal symmetry because of powder-averaged intensities [15]. The typical results at $T = 12.0$ K and $T = 2.0$ K in Figs. 4(a) and 4(b) indicate that FM ordering with the spin components in the ab plane (M_{ab}) and along the c axis (M_c) fits the experimental data by combining the two IRs, $m\Gamma_2^+ \oplus m\Gamma_6^+$. The refined spin components are $M_{ab} = 4.16(4)\mu_B$ and $M_c = 5.31(6)\mu_B$ at $T = 2.0$ K, where the angle at which the spins are tilted from the ab plane toward the c axis is $\phi = 51.9(5)^\circ$ at $T = 2.0$ K. The refined total magnetic moment is $M = 6.75(7)\mu_B$ per Ho^{3+} ion at $T = 2.0$ K, which is smaller than the maximum ordered moment associated with the Ho^{3+} ion. This indicates that the value of the magnetic moment is affected by interactions in the crystalline electric field (CEF).

The temperature dependence of the total magnetic moment also shows a kink anomaly at $T_2 = 11$ K, as shown by the arrow in Fig. 3(c). The temperature dependence of the angle ϕ is shown in Fig. 3(b), which reveals that ϕ is almost constant below $T \leq 11$ K, whereas it significantly varies with temperature in the intermediate-temperature phase ($11 \text{ K} \leq T \leq 15 \text{ K}$). These results imply that the second phase transition at

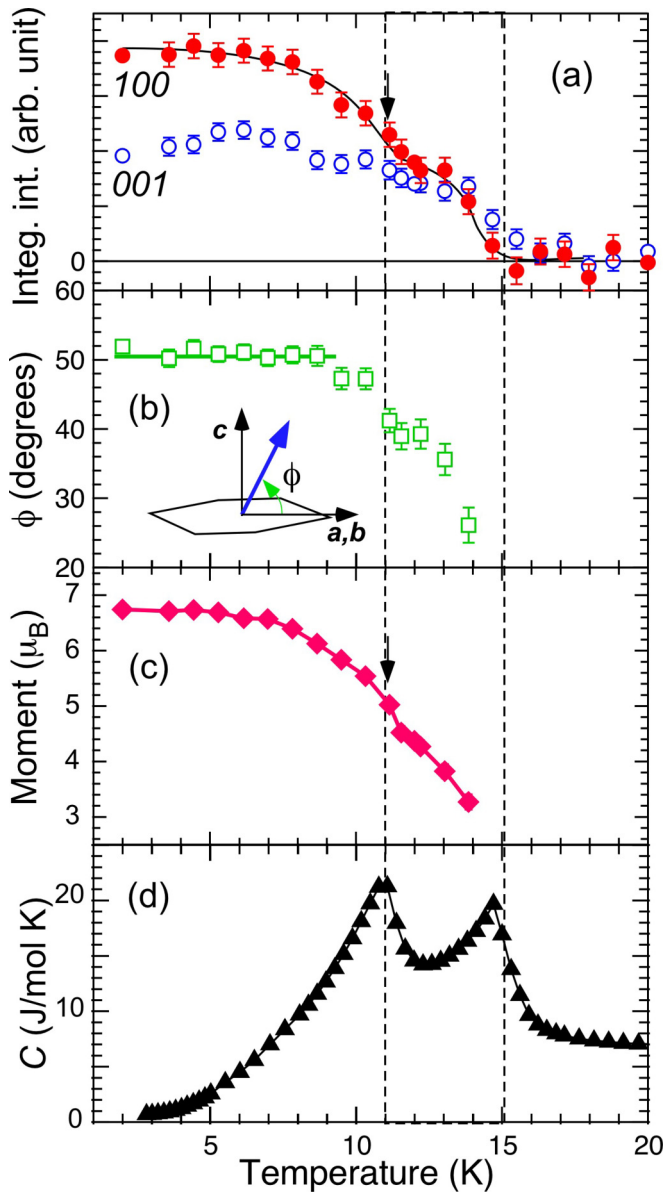


FIG. 3. Temperature dependence of the (a) integrated intensities of the magnetic 001 and 100 reflections and (b) tilting angle of the refined spin direction from the a axis toward the c axis, (c) total magnetic moment, and (d) specific heat in HoB_2 .

$T_2 = 11$ K, the existence of which is also proved by the peak anomaly in the specific heat data shown in Fig. 3(d), is associated with the changes in both the total magnetic moment and the spin orientation. These spin behaviors are similarly seen in compounds with magnetic and quadrupole orderings [16,17], which will be discussed in Sec. IV.

Since the spin direction in the basal plane could not be determined by the neutron powder diffraction experiment, three possible magnetic structures with the refined spin components $M_{ab} = 4.16(4)\mu_B$ and $M_c = 5.31(6)\mu_B$ exist for HoB_2 and are summarized in Fig. 5. It should be noted that a neutron diffraction experiment with a single crystal is able to determine the spin direction in the basal plane. For the structures with magnetic moments of either $\mathbf{M} = (M_a, 0, M_c)$ [Fig. 5(a)]

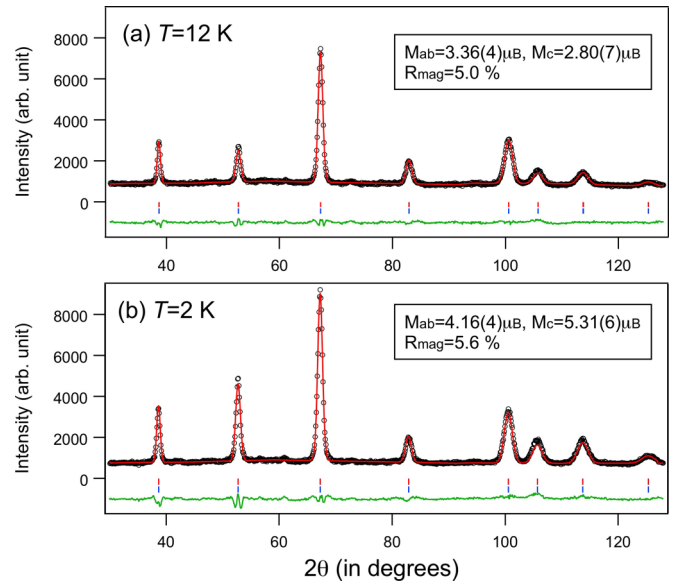


FIG. 4. Results of Rietveld refinements of the data measured at (a) $T = 12$ K and (b) $T = 2.0$ K for HoB_2 . The insets in (a) and (b) show the refined parameters and the reliable factor for the magnetic Bragg reflections. The upper and lower vertical bars denote the positions of nuclear and magnetic reflections, respectively.

or $\mathbf{M} = (M_a, -M_a, M_c)$ [Fig. 5(b)], the threefold and sixfold rotational symmetries in the $P6/mmm$ space group are broken, and the system maintains twofold rotation and a mirror plane, combined with a time-reversal operation. It leads to the possible magnetic space group $C2'/m'$. In the case of the structure with the spins aligned in the general direction $\mathbf{M} = (M_a, M_b, M_c)$, the system loses all the symmetry elements in $P6/mmm$ apart from inversion, $\bar{1}$, leading to the possible magnetic space group $P\bar{1}$. Consequently, the possible

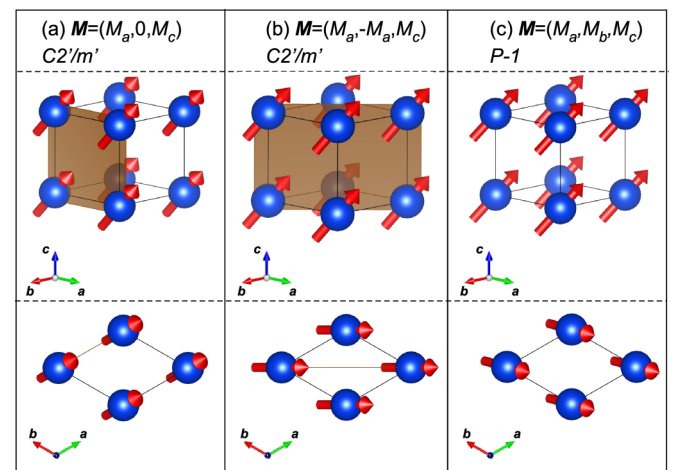


FIG. 5. Possible magnetic structure represented by the combination of the two magnetic irreducible representations, $\Gamma_2^+ \oplus \Gamma_6^+$. The spin components are allowed by magnetic moments along the hexagonal $[101]$ in (a), $[1\bar{1}1]$ in (b), and general direction in (c). For the first two cases in (a) and (b), the resultant magnetic space group is $C2'/m'$. For the case in (c), it becomes $P\bar{1}$. The brown plane denotes a plane on which spins are lying.

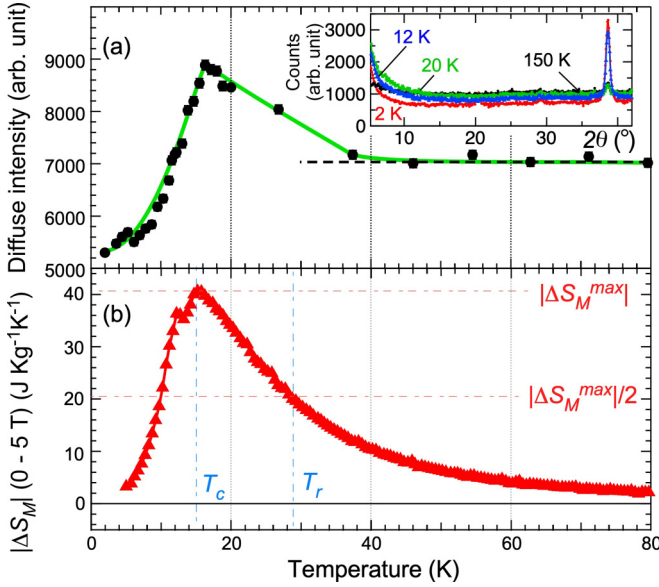


FIG. 6. (a) Temperature dependence of diffuse scattering intensity integrated for the scattering angle between 5.3° and 11° in the neutron diffraction pattern of HoB_2 . The inset shows the neutron diffraction patterns at typical temperatures, 2.0, 12, 20, and 150 K. (b) Temperature dependence of the magnetic entropy changes between zero field and at 5 T in HoB_2 . The entropy was estimated from the magnetization curves plotted using measurements recorded in the present work. Dashed lines show T_C and T_r at which the maximum $|\Delta S_M|$ becomes the half value above T_C .

magnetic space groups for these structures are either $C2'/m'$ [Figs. 5(a) and 5(b)] or $P\bar{1}$ [Fig. 5(c)].

B. Ferromagnetic short-range order

As shown in the inset of Fig. 6(a), temperature-dependent diffuse scattering is observed in the low- Q region. Estimating the diffuse scattering intensity by integrating the intensity in the low- Q region ($5.3^\circ \leq 2\theta \leq 11^\circ$), we obtain the temperature dependence of the diffuse scattering shown in Fig. 6(a). Above $T \sim 40$ K, the diffuse scattering intensity is constant [the dotted line in Fig. 6(a)], while it is significantly enhanced below $T \sim 40$ K. The diffuse scattering above T_C can be analyzed using a first-order approximation of the short-range-order formula [18]

$$\frac{d\sigma}{d\omega} = \frac{2}{3} \left(\frac{\gamma r_0}{2} \right)^2 \mu_{\text{eff}}^2 f_m^2 \left(1 - \frac{2\mu_{\text{eff}}^2}{3k_B T} \sum_n J_n z_n \frac{\sin X_n}{X_n} \right), \quad (1)$$

where $d\sigma/d\omega$ is the differential-scattering cross section in barns per steradian per Ho^{3+} . The first and second terms represent the paramagnetic scattering and short-range order. $\gamma r_0/2 = 0.2695 \times 10^{-12}$ cm ($r_0 = e^2/m_e c^2$ is the classical electron radius, e and m_e are the charge and mass of an electron, and c is the velocity of light); μ_{eff} is the effective Bohr magneton number of the disordered moment in μ_B . J_n is proportional to the exchange interaction between a given atom and the n th neighboring atom; z_n is the coordination number of the n th neighbors. $X_n = 4\pi r_n \sin \theta / \lambda$, and r_n is the n th neighboring distance.

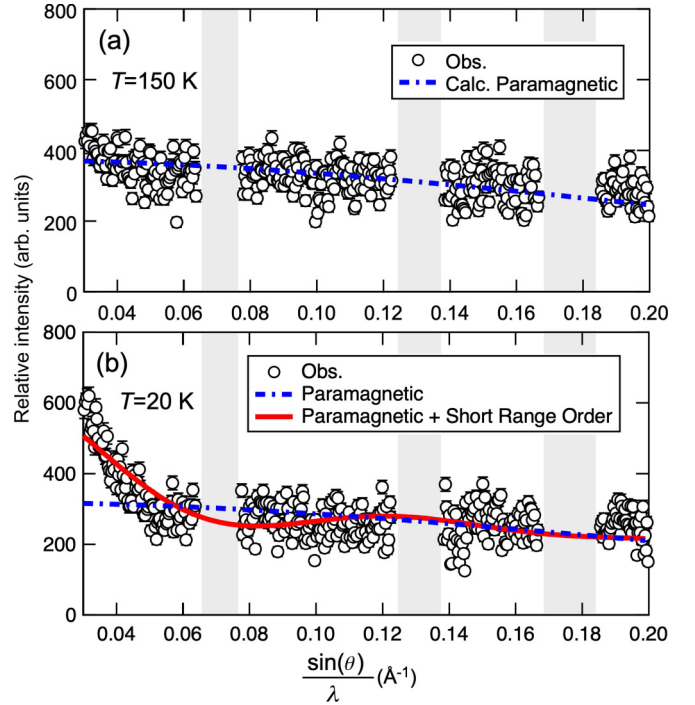


FIG. 7. Comparison between observed and calculated neutron intensities for the data at (a) 150 K and (b) 20 K. The data at $T = 2$ K is subtracted from those at $T = 20$ K, apart from the Bragg reflection positions masked by shading. The calculated curves represent the paramagnetic (dashed line) and short-range order (solid line), which are represented by the first and second terms in Eq. (1), respectively. For $T = 150$ K, the refined magnetic moment is $\mu_{\text{eff}} = 7.3(1)\mu_B$. For $T = 20$ K, $J_1 = -0.22(1)k_B$, $J_2 = -0.16(4)k_B$, $J_3 = -0.28(1)k_B$, and $\mu_{\text{eff}} = 6.75\mu_B$.

Since the neutron intensity at $T = 150$ K gradually decreases with increasing Q , the first term (paramagnetic scattering) can fit the observed intensity [Fig. 7(a)]. In this analysis, in order to obtain a pure magnetic contribution from the experimental data, the intensity data at $T = 2$ K (apart from the Bragg reflections) are subtracted from those at (a) $T = 150$ K and (b) $T = 20$ K as the background originating from nuclear incoherent scattering. The experimental data at $T = 20$ K show large diffuse intensity for $\sin(\theta)/\lambda < 0.05 \text{ \AA}^{-1}$, which corresponds to the second term (short-range order) shown in Fig. 7(b). In order to estimate the exchange parameters J_n , we tested some sets of J_n so that they fit the experimental data. The n th atomic sites up to $n = 3$ are defined as $\mathbf{r}_n = \{(1, 0, 0), (0, 0, 1), (1, 0, 1)\}$ ($z_n = \{6, 2, 12\}$). For the case with exchange interactions up to the third neighbors ($n = 1, 2, 3$), we can explain the experimental data [solid line in Fig. 7(b)]. In this calculation, μ_{eff} is fixed to the low-temperature value, $6.75\mu_B$. The exchange interaction parameters are refined to be $J_1 = -0.22(1)k_B$, $J_2 = -0.16(4)k_B$, and $J_3 = -0.28(1)k_B$, where the minus sign represents a FM interaction. These results indicate that the FM short-range order exists, which is caused by the FM exchange interactions.

The diffuse scattering corresponding to the short-range order appears below $T \sim 40$ K, as shown in Fig. 6(a). It shows a maximum at $T = 16$ K. The behaviors in the diffuse scattering intensity are similar to those of the magnetic

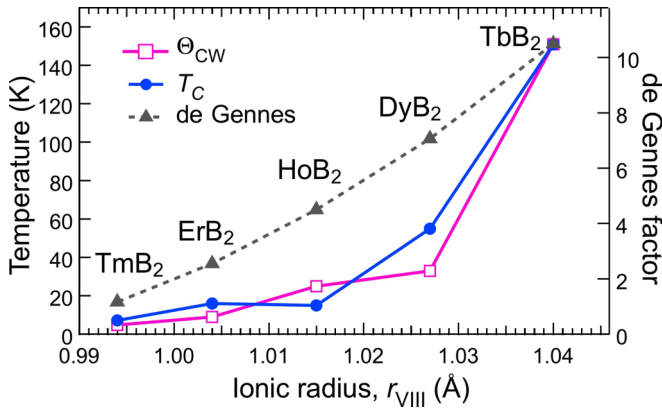


FIG. 8. Ionic radius (trivalent) dependence of the Curie-Weiss temperature Θ_{CW} , Curie temperature T_C , and de Gennes factor $(g - 1)^2 J(J + 1)$ (g is the Landé g factor, and J is the total angular momentum quantum number). The de Gennes factor was normalized to the value of TbB_2 .

entropy change $|\Delta S_M|$, which also shows a large enhancement below $T \sim 40$ K and shows the maximum, $|\Delta S_M| = 40.1 \text{ J kg}^{-1} \text{ K}^{-1}$, at $T = 16$ K [Fig. 6(b)]. From the experimental facts, we conclude that the FM short-range order, rather than the long-range order, is strongly related to $|\Delta S_M|$.

IV. DISCUSSION

The origin of the large $|\Delta S_M|$ in HoB_2 , compared with that of other rare-earth diborides, is worthy of discussion. As shown in Fig. 8, the Curie-Weiss temperature Θ_{CW} and T_C are drastically lowered as the ionic radius decreases from Tb to Tm [5–9], and Θ_{CW} becomes antiferromagnetic (AFM) in YbB_2 [19]. The T_C 's in RB_2 are significantly lower than those predicted by the de Gennes factor [20], which describes transition temperatures for rare-earth compounds [21–23]. These facts imply the existence of FM and AFM exchange interactions in RB_2 , which is expected on the basis of the Ruderman-Kittel-Kasuya-Yoshida indirect exchange interactions that are known to exist in metallic systems [24–26]. In fact, the ground state energy of the FM state in HoB_2 was reported to closely approximate that of the AFM state in previous density functional theory calculations of the rare-earth diborides [27].

Suppression of the FM long-range order as a result of the competing exchange interactions in HoB_2 is expected to make the FM short-range order exist above T_C , as was actually observed in the present neutron diffraction experiment. The FM short-range correlation results in high FM susceptibility, which is responsible for the large magnetization enhancement induced by the magnetic field, even in the paramagnetic phase. A neutron diffraction experiment under a magnetic field is needed to study the magnetic field dependence of the FM short-range order. A factor T_r/T_C ($T > T_C$), where $|S_M|/|S_M^{\text{max}}| = 0.5$ at T_r [Fig. 6(b)], was introduced to roughly estimate the extent to which the large value of $|\Delta S_M|$ is maintained at high temperature. In the case of HoB_2 , the value of T_r/T_C was estimated to be ~ 1.9 . This value for HoB_2 is larger than that of typical MCE materials; for example,

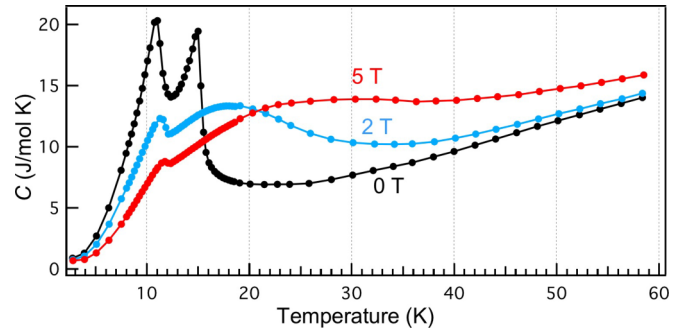


FIG. 9. Temperature dependence of specific heat at typical magnetic fields of 0, 2, and 5 T. The data were taken from Ref. [5].

the corresponding values are ~ 1.3 for DyAl_2 [4], ~ 1.7 for HoAl_2 [4], and ~ 1.7 for HoN [28]. This suggests the high FM fluctuation caused by the competing interactions is the origin of the large $|\Delta S_M|$ in HoB_2 .

As described in the Introduction, HoB_2 shows two phase transitions, i.e., at $T = 15$ K and $T = 11$ K, both of which are clearly observed in the specific heat data [Fig. 3(d)]. DyB_2 also exhibits successive phase transitions at $T = 50$ K and $T = 20$ K [9]. Although the lower phase transition of DyB_2 was suggested to be a spin-reorientation-like transition, the detail of the transition has not been clear so far. Conversely, the other rare-earth diborides RB_2 ($R = \text{Tb}, \text{Er}, \text{Tm}$) exhibit only a single phase transition [6–8].

The phase transition at $T = 15$ K in HoB_2 corresponds to the transition from the paramagnetic to the FM phase, which was proved by the magnetization measurement in a previous study [5]. The existence of the phase transition at $T_2 = 11$ K was confirmed by our neutron diffraction measurement, which showed that the spin direction starts to change and the temperature dependence of the total magnetic moment shows the kink anomaly at T_2 [Figs. 3(b) and 3(c)], and $|\Delta S_M|$ also shows a double-peak feature shown in Fig. 6(b). The peak at T_2 gives an additional contribution to the maximum value of $|\Delta S_M|$ in HoB_2 . Although the contribution associated with the lower transition cannot be estimated quantitatively, we can infer that the large $|\Delta S_M|$ in HoB_2 is realized by adding the contribution around the second phase transition. Actually, DyB_2 shows two broad peaks in the temperature dependence of $|\Delta S_M|$ at the higher and lower transition temperatures at $T = 50$ K and $T = 20$ K, respectively [9]. Since these two contributions do not overlap each other due to the well-separated transition temperatures, one can see that the contribution at the lower transition ($\sim 10.5 \text{ J kg}^{-1} \text{ K}^{-1}$) is comparable to the maximum value of $|\Delta S_M| = 17 \text{ J kg}^{-1} \text{ K}^{-1}$ in DyB_2 .

These phase transitions in HoB_2 show distinct differences in the magnetic field H dependences of the thermal variation of the specific heat, as shown in Fig. 9 [5]. The sharp peak anomaly at $T = 15$ K and $H = 0$ T rapidly broadens as H increases to 5 T; the peak also undergoes a significant shift as a result of the magnetic field. FM systems typically experience broadening of the peaks of the specific heat in the presence of a magnetic field [29], proving the paramagnetic to FM phase transition at $T = 15$ K. Conversely, the intensity of the peak representing the phase transition at $T = 11$ K and $H = 0$ T

is weakened but remains well resolved even at $H = 5$ T; the transition temperature is slightly shifted to $T = 11.7$ K at $H = 5$ T. Thus, the H dependences of these two peak anomalies are completely different from each other, suggesting that these phase transitions originate from different degrees of freedom.

The aforementioned situation is typically observed in systems that show magnetic and quadrupolar ordering, e.g., the system RB_2C_2 ($R = \text{Dy}$ and Ho) [30,31]. In these compounds, the magnetic field also affects the specific heat anomaly associated with the quadrupolar ordering to a lesser degree than that associated with the magnetic ordering. In addition, the spin orientation and the total magnetic moment also show anomalies at T_2 [Figs. 3(b) and 3(c)], which can be caused by the temperature change in the crystal field interaction. These behaviors are similarly seen in the compounds with magnetic and quadrupolar orderings, such as DyB_4 [16] and NpRhGa_5 [17]. In HoB_2 , the $4f^{10}$ electronic state of Ho^{3+} with $J = 8$ splits into 11 multiplets in the CEF with hexagonal point group symmetry D_{6h} at the Ho site [32,33]. Although the energy level scheme of the CEF and the ground state are still unknown, certain multiplets could possess a quadrupole moment that can be ordered. We thus suggest that the phase transition at T_2 in HoB_2 possibly has its origins in a kind of quadrupolar ordering. In a recent paper on MCE in RB_4 ($R = \text{Dy}$, Ho), it was reported that strong coupling between magnetic ordering and quadrupolar ordering can affect the MCE [34]. For a more exact understanding of the second phase transition in HoB_2 , inelastic neutron scattering and resonant x-ray scattering experiments with a single crystal are required.

V. CONCLUSION

In conclusion, we investigated the spin orderings associated with the recently discovered gigantic magnetocaloric effect in HoB_2 by carrying out a neutron diffraction experiment. With respect to the long-range FM ordering, the spin direction is not parallel to the hexagonal axes and is temperature dependent in the intermediate-temperature phase ($11 \text{ K} \leq T \leq 15 \text{ K}$). The temperature dependence of the total magnetic moment shows the kink anomaly at the second transition temperature, which is typically seen in the compounds with quadrupolar ordering [16,17]. The short-range FM ordering, which developed below ~ 40 K with a maximum at 16 K, is strongly related to the large magnetic entropy change. From these experimental results, we inferred that (i) the spin reorientation transition, which is likely associated with quadrupolar ordering, giving the additional contribution to $|\Delta S_M|$ at the lower phase transition temperature, $T = 11$ K, and (ii) the large FM fluctuation above T_C , with its origins in the strong suppression of the FM long-range order, are the likely causes of the gigantic magnetic entropy change in HoB_2 .

ACKNOWLEDGMENTS

The images in Figs. 1 and 5 were created by the software VESTA developed by K. Momma [35]. The neutron diffraction experiment was performed with the approval and support of the Institut Laue Langevin. This work was supported by JSPS KAKENHI Grants No. 17KK0099, No. 19H02177, No. 19H04400, and No. 20K05070 and JST-Mirai Program Grant No. JPMJMI18A3, Japan.

-
- [1] V. K. Pecharsky and K. A. Gschneidner, Jr., *J. Magn. Magn. Mater.* **200**, 44 (1999).
 - [2] T. Numazawa, K. Kamiya, T. Utaki, and K. Matsumoto, *Cryogenics* **62**, 185 (2014).
 - [3] H. Wada, Y. Tanabe, M. Shiga, H. Sugawara, and H. Sato, *J. Alloys Compd.* **316**, 245 (2001).
 - [4] P. J. von Ranke, N. A. de Oliveira, M. V. Tovar Costa, E. P. Nobrega, A. Caldas, and I. G. de Oliveira, *J. Magn. Magn. Mater.* **226–230**, 970 (2001).
 - [5] P. Baptista de Castro, K. Terashima, T. D. Yamamoto, Z. Hou, S. Iwasaki, R. Matsumoto, S. Adachi, Y. Saito, P. Song, H. Takeya, and Y. Takano, *NPG Asia Mater.* **12**, 35 (2020).
 - [6] Z. Han, D. Li, H. Meng, X. H. Liu, and Z. D. Zhang, *J. Alloys Compd.* **498**, 118 (2010).
 - [7] K. H. J. Buschow, *Boron and Refractory Borides* (Springer-Verlag, Berlin-Heidelberg-New York, 1977), pp. 494–515.
 - [8] T. Mori, T. Takimoto, A. Leithe-Jasper, R. Cardoso-Gil, W. Schnelle, G. Auffermann, H. Rosner, and Yu. Grin, *Phys. Rev. B* **79**, 104418 (2009).
 - [9] H. Meng, B. Li, Z. Han, Y. Zhang, X. Wang, and Z. Zhang, *Sci. China Technol. Sci.* **55**, 501 (2012).
 - [10] D. Okuyama, T. Matsumura, K. Iwata, and Y. Murakami, *J. Magn. Magn. Mater.* **310**, e152 (2007).
 - [11] A. Boutahar, R. Moubah, E. K. Hlil, H. Lassri, and E. Lorenzo, *Sci. Rep.* **7**, 13904 (2017).
 - [12] I. P. Orench, J. F. Clergeau, S. Martínez, M. Olmos, O. Fabelo, and J. Campo, *J. Phys.: Conf. Ser.* **549**, 012003 (2014).
 - [13] J. Rodriguez-Carvajal, *Phys. B (Amsterdam, Neth.)* **192**, 55 (1993).
 - [14] B. J. Campbell, H. T. Stokes, D. E. Tanner, and D. M. Hatch, *J. Appl. Crystallogr.* **39**, 607 (2006).
 - [15] G. Shirane, *Acta Crystallogr.* **12**, 282 (1959).
 - [16] T. Matsumura, D. Okumura, T. Mouri, and Y. Murakami, *J. Phys. Soc. Jpn.* **80**, 074701 (2011).
 - [17] F. Honda, N. Metoki, K. Kaneko, S. Jonen, E. Yamamoto, D. Aoki, Y. Homma, Y. Haga, Y. Shiokawa, and Y. Onuki, *Phys. Rev. B* **74**, 144413 (2006).
 - [18] M. Slotnik, *Phys. Rev.* **83**, 1226 (1951).
 - [19] M. A. Avila, S. L. Budko, C. Petrovic, R. A. Ribeiro, P. C. Canfield, A. V. Tsvyashchenko, and L. N. Fomicheva, *J. Alloys Compd.* **358**, 56 (2003).
 - [20] P. G. Gennes, *C. R. Acad. Sci. Paris* **247**, 1836 (1958).
 - [21] K. Inoue, Y. Nakamura, A. V. Tsvyashchenko, and L. Fomicheva, *J. Phys. Soc. Jpn.* **64**, 2175 (1995).
 - [22] J. L. Wang, C. Marquina, M. R. Ibarra, and G. H. Wu, *Phys. Rev. B* **73**, 094436 (2006).
 - [23] R. M. Bozorth, *J. Appl. Phys.* **38**, 1366 (1967).
 - [24] M. A. Ruderman and C. Kittel, *Phys. Rev.* **96**, 99 (1954).
 - [25] T. Kasuya, *Prog. Theor. Phys. Kyoto* **16**, 45 (1956).
 - [26] K. Yosida, *Phys. Rev.* **106**, 893 (1957).

- [27] S. Kacimi, B. Bekkouche, A. Boukortt, F. Zazoua, M. Djermouni, and A. Zaoui1, *Phys. Status Solidi B* **249**, 1470 (2012).
- [28] T. A. Yamamoto, T. Nakagawa, K. Sako, T. Arakawa, and H. Nitani, *J. Alloys Compd.* **376**, 17 (2004).
- [29] N. M. Hong, N. P. Thuy, G. Schaudy, T. Holubar, G. Hilscher, and J. J. M. Franse, *J. Appl. Phys.* **73**, 5698 (1993).
- [30] T. Ohmori, A. Tobo, H. Ymauchi, H. Onodera, and Y. Yamaguchi, *J. Phys. Soc. Jpn.* **71**, 80 (2002).
- [31] K. Indoh, A. Tobo, H. Ymauchi, K. Ohoyama, and H. Onodera, *J. Phys. Soc. Jpn.* **73**, 669 (2004).
- [32] E. A. Gotemychk, E. Muhle, B. Lippold, D. Chistyakov, and E. M. Savitsk, *Phys. Status Solidi B* **127**, 371 (1985).
- [33] Y. Andoh, *J. Phys. Soc. Jpn.* **56**, 4075 (1987).
- [34] M. S. Song, K. K. Cho, B. Y. Kang, S. B. Lee, and B. K. Cho, *Sci. Rep.* **10**, 803 (2020).
- [35] K. Momma and F. Izumi, *J. Appl. Crystallogr.* **41**, 653 (2008).